Biosensors and Bioelectronics 126 (2019) 339–345

Contents lists available at ScienceDirect

Biosensors and Bioelectronics

journal homepage: www.elsevier.com/locate/bios

Auto-cleaning paper-based electrochemiluminescence biosensor coupled with binary catalysis of cubic Cu_2O-Au and polyethyleneimine for quantification of Ni^{2+} and Hg^{2+}

Yuzhen Huang[a], Li Li[a], Yan Zhang[a,b], Lina Zhang[c,*], Shenguang Ge[d], Jinghua Yu[a,*]

[a] School of Chemistry and Chemical Engineering, University of Jinan, Jinan 250022, PR China
[b] School of Materials Science and Engineering, University of Jinan, Jinan 250022, PR China
[c] Shandong Provincial Key Laboratory of Preparation and Measurement of Building Materials, University of Jinan, Jinan 250022, PR China
[d] Institute for Advanced Interdisciplinary Research, University of Jinan, Jinan 250022, PR China

ARTICLE INFO

Keywords:
Electrochemiluminescence
Auto-cleaning
Paper-based device
Cu_2O-Au
Heavy metal ion
N-(4-Aminobutyl)-N-ethylisoluminol

ABSTRACT

Inspired by the pop-up greeting cards, a 3D collapsible auto-cleaning paper-based electrochemiluminescence (ECL) biosensor (CAPEB) with different functions of signal collection and residual multiple cleaning, is developed for sensitive detection of Ni^{2+} and Hg^{2+} by simply regulating its 3D configurations. The multiple fluidic paths and the hollow-channel structure were firstly integrated into the paper substrate, realizing simultaneously repetitive auto-cleaning of the two working electrodes. For achieving ultrasensitive Ni^{2+} and Hg^{2+} monitoring, binary catalysis consisting of the intermolecular co-reaction (H_2O_2 and N-(4-Aminobutyl)-N-ethylisoluminol (ABEI)) and intramolecular catalysis (polyethyleneimine (PEI)-ABEI) was introduced. Specifically, silver nanospheres with a large specific surface area and excellent conductivity were grown on the paper working electrode and served as the sensor substrate for fixing PEI-ABEI and Ni^{2+}-specific DNAzyme. With the assistance of DNAzyme, Cu_2O-Au and ferrocene (Fc) labeled strand S2 were immobilized on electrode surface through the hybridization reaction, and catalyzed H_2O_2 to generate reactive oxygen species, promoting the luminescence of ABEI. In the existence of Ni^{2+}, DNAzyme was activated followed by cleavage of strand S2 to induce the release of Fc, which quenched the ECL signal of ABEI, eventually realizing the detection of Ni^{2+}. Similarly, for sensitive quantification of Hg^{2+}, full thymine (T) bases strand S3 was modified on surface of Cu_2O-Au and anchored Hg^{2+} by T-Hg^{2+}-T pairing interaction. The ECL intensity was decreased along with increasing of Hg^{2+} due to the quenching effect of Hg^{2+} on ECL emission of ABEI. Based on this ingenious system, the detection of Ni^{2+} and Hg^{2+} had high sensitivity, wide linear ranges, and low detection limits. The results indicated that the integration of a multi-channel structure into a paper device chips opened new opportunities for designing promising paper-based devices for metal ions diagnosis.

1. Introduction

Heavy metal ions (HMI) (Ge and Li, 2018) are considered as the highly toxic micropollutants and represent a growing environmental problem. HMI, especially mercury ion (Hg^{2+}) or nickel ion (Ni^{2+}), with excessive levels in aquatic ecosystems have a tendency to accumulate over time in living organisms through the food chain, which can cause various disease including cancers of the respiratory, hepatic, digestive systems, and even death (Koley et al., 2016). Therefore, the ultrasensitive quantification of HMI both in vitro and in vivo is imperative to meet the needs of environmental monitoring and clinical detection (Huang et al., 2014). Over the past years, many efforts have been devoted to develop ultrasensitive HMI detection strategies like fluorescence (Ajayaghosh et al., 2005; Guo et al., 2004; Xie et al., 2010), colorimetric detection (Hai et al., 2018; Li et al., 2016; Zhang et al., 2017a), atomic absorption spectroscopy (Liu et al., 2013), electrochemical (Cui et al., 2015; Miao et al., 2017; Zhang et al., 2015), and electrochemiluminescence (ECL) methods (Zhang et al., 2013). Among these technologies, ECL possessing the advantages of high reproducibility, controllability, and sensitivity (Dong et al., 2017; Ke et al., 2018; Yan et al., 2018) is known as a promising analytical method for microsample analysis. Yet, certain technological challenges still remain in ECL methodologies such as requirement of large-scale instruments and multiple manual operations. Therefore, there is a strong need to

* Corresponding authors.
E-mail addresses: mse_zhangln@ujn.edu.cn (L. Zhang), chm_yujh@ujn.edu.cn (J. Yu).

https://doi.org/10.1016/j.bios.2018.11.008
Received 8 September 2018; Received in revised form 20 October 2018; Accepted 5 November 2018
Available online 06 November 2018
0956-5663/

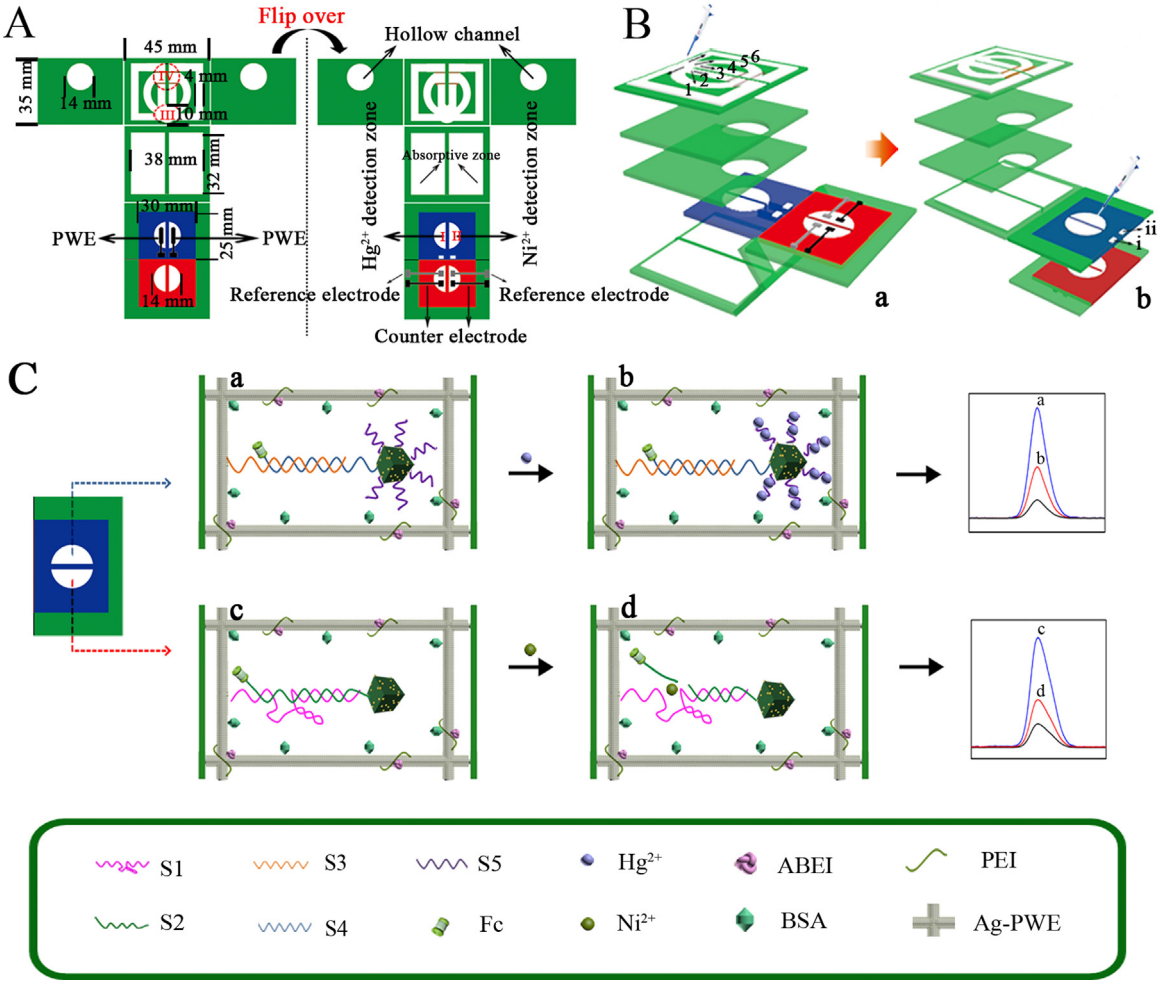

Scheme 1. Patterns for (A) wax-printing and (B) folding of the 3D CAPEB. (C) Illustration of the fabrication procedures and detection process for CAPEB.

develop a simple, cheap, high-efficiency, and multifunctional integrated device for ultra-sensitive detection of HMI.

Paper (Martinez et al., 2010; Zhang et al., 2017b) as one of the truly ubiquitous manmade materials in modern society has attracted considerable attention and is regarded as a significant eco-friendly substrate exploiting for various analysis fields including environmental monitoring, chemical detection, and clinical testing (Channon et al., 2018; Li et al., 2017; Weng and Neethirajan, 2018; Yang et al., 2018a) because of their low-cost, portability, retrievability, designability, foldability, and hydrophilicity (Cai et al., 2018; Huang et al., 2016; Kong et al., 2018). However, further development of the paper-based analytical device has so far been constrained by tedious manual washing steps and limited detection sensitivity. To address these challenges, a novel paper chip with multiple auto-cleaning properties was developed, in which a “crown” shape fluidic channel was ingenious designed. Under the help of the capillary action of the paper cellulosic fibers, the added buffer solution was diverted into different channels with various lengths, enabling the repetitive washing of the paper working zones at different times. To obtain an enhanced sensitivity, binary catalysis consisting of the intermolecular co-reaction between N-(4-Aminobutyl)-N-ethylisoluminol (ABEI) and H_2O_2 and intramolecular catalysis of self-catalyzed ABEI-based molecule was introduced into this paper device. Polyethyleneimine (PEI), as a high-molecular polymer with abundant amine co-reactive groups, has more outstanding catalytic effect for the ECL of ABEI than some co-reactive small molecules (Wang et al., 2018). Based on the consideration, PEI connected with ABEI was employed as the self-catalyzed molecule for the ECL intramolecular reaction. As for the ABEI-H_2O_2 system (Li et al., 2018; Liu et al., 2014), nanomaterial with features of high catalytic activity, easy storage, and low cost, was reported as catalysts for ECL amplification frequently (Bao et al., 2018; Fang et al., 2017; Yang et al., 2018b). Especially for Cu_2O-Au nanomaterial (Hua et al., 2011; Liu, 2011; Susman et al., 2014; Xu et al., 2009), as a kind of composite materials, it presents superior peroxidase-like activity that catalyzes H_2O_2 decomposition to generate abundant reactive oxygen species (ROSs) for enhancing the ECL emission of ABEI. Besides, Cu_2O-Au can also achieve high DNA loading density on account of its large surface area (Chen et al., 2018). Therefore, Cu_2O-Au was introduced into the system to promote the ECL intermolecular co-reaction.

Herein, we constructed a collapsible auto-cleaning paper-based ECL biosensor (CAPEB). Profiting from the multiple fluidic paths, CAPEB, with two different 3D configurations, had the functions of auto-cleaning and signal collection. To show its practical applicability, CAPEB was designed for the detection of Ni^{2+} and Hg^{2+} by serving ABEI as luminous agent. Silver nanoparticles grown on the surface of paper working electrode (Ag-PWE) were fabricated for covalently anchoring functional materials. In the absence of target, a strong initial ECL signal was achieved by the binary catalysis strategies including (i) intramolecular catalysis of PEI-ABEI and (ii) intermolecular co-reaction between H_2O_2 and ABEI in the same ECL process. Duo to their excellent catalytic performance for H_2O_2, cubic Cu_2O-Au and Fc were employed as the enhancer of intermolecular co-reaction. The analysis of Ni^{2+} was achieved via induced activation of DNAzyme. The complementary chain was broken by activated Ni^{2+}-specific DNAzyme, and Fc was dropped from the surface of the electrode, resulting in a relatively weak signal. Besides, the detection of Hg^{2+} was realized by T-Hg^{2+}-T pairing

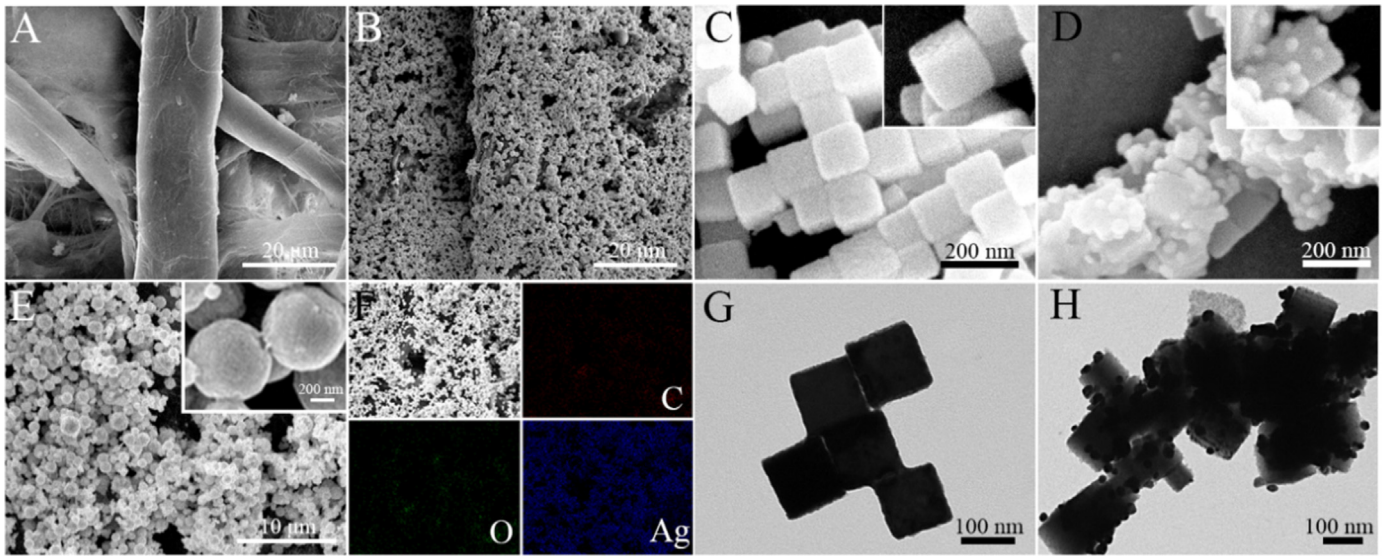

Fig. 1. SEM images of (A) bare paper, (B) Ag-PWE, (C) Cu_2O, (D) Cu_2O-Au, and (E) enlarged Ag-PWE. (F) The element mapping of the Ag-PWE. TEM images of (G) Cu_2O and (H) Cu_2O-Au.

interaction. With the assistance of full thymine bases DNA strand, Hg^{2+} was fixed on the surface of electrode. A weak ECL signal was obtained because Hg^{2+} had an efficient quenching effect on the ECL of ABEI. Under the optimal conditions, CAPEB exhibited excellent analytical performance for the detection of Ni^{2+} and Hg^{2+} with detection limits of 3.1 nM and 3.8 pM. Meanwhile, this work opens a different perspective for design of paper-based device and provides a novel format for the analysis of HMI.

2. Experimental section

2.1. Design of the CAPEB

CAPEB was elaborately designed referring to our previous work with slight modification (Ge et al., 2018; Yang et al., 2017; Zheng et al., 2018). The fabrication procedure was represented in the Supporting information. Photographs of real product were added in the Fig. S1B. The entire CAPEB consisted of one working tab, one counter tab, one multipass tab, two assistant tabs, and one adsorptive tab (Fig. S1B, part a). And the detailed sizes of CAPEB were shown in Scheme 1A. Two semicircular hydrophilic zones for analysis of Ni^{2+} and Hg^{2+} were designed on the working tab, which offered zones for layer-by-layer modification. Carbon working electrodes were coated on another side of semicircular hydrophilic zones to get paper working electrode (PWE). The carbon counter electrodes as well as Ag/AgCl reference electrodes were screen-printed on two hydrophilic zones of the counter tab, respectively. After folding the counter tab along the black line (between the counter tab and the working tab), the electrochemical cell was formed when CAPEB was filled with the buffer solution, and the detailed 3D configuration was shown in the Scheme 1B, part b. Additionally, in order to achieve simultaneous auto-cleaning of the two working electrodes, a multi-channel structure with “crown” shape (Scheme 1A) was tactfully designed. The added buffer solution would flow from the zone III to the zone IV through six channels with different lengths (Scheme 1B, part a, 1–6). Prior to the washing steps, the working tab should be folded and placed in the next layer of two assistant tabs as the Scheme 1B, part a. Two semicircular zones exactly aligned with circular hollow channel on two assistant tabs, and the zone IV on the multipass tab. Therefore, the washing buffer reaching the zone IV would flow to the two semicircular PWEs along the circular hollow channel due to gravitational effects. The buffer spread over the whole PWEs on account of capillary action. Meanwhile, with the help of attraction of the bottom hydrophilic paper fiber, the buffer was assimilated and removed in the adsorptive tab. Besides, it was worth mentioning that two assistant tabs were designed to improve the interval between the multipass tab and the working tab, which effectively prevented reflux of buffer.

2.2. Preparation of Ag-PWE, PEI-ABEI@Ag-PWE, cubic Cu_2O-Au, Fc-S2-Cu_2O-Au, and Fc-S4-Cu_2O-Au-S5

The detailed preparation procedures of Ag-PWE, PEI-ABEI@Ag-PWE, cubic Cu_2O-Au, Fc-S2-Cu_2O-Au, and Fc-S4-Cu_2O-Au-S5 were described in the Supplementary information. The corresponding schematic diagrams of fabrication process of Fc-S2-Cu_2O-Au and Fc-S4-Cu_2O-Au-S5 were shown in Scheme S1.

2.3. Fabrication process of CAPEB

The detailed procedure was described in the Supplementary information, and the corresponding schematic diagram was shown in Scheme 1C.

2.4. Analysis of CAPEB

First, the device was folded as shown in Scheme 1B, part b. The CAPEB was placed in an ECL detector cell after dropping 30 μL of 10 mM Tris-HCl buffer (pH 7.4, 1 mM H_2O_2). The potential scanning range was from 0.2 to 0.8 V with a scanning rate of 200 mV s^{-1}. The initial ECL signal of the zone I was measured and denoted as I_0. Similarly, the signal intensity obtained from the zone II was denoted as I_0'. Then, Ni^{2+} and Hg^{2+} solution with different concentrations were prepared in the Tris-HCl buffer by serial dilution. 20 μL of Hg^{2+} solution was dropped on the zone I and incubated on the surface of electrode for 90 min at room temperature. And on the surface of the zone II, 20 μL of Ni^{2+}solution was incubated for 60 min. After that, the device was folded into the configuration as the Scheme 1B, part a. Tris-HCl buffer was dropped on the zone III to finish the washing step and dried at room temperature. Finally, the PWEs were connected into the circuit to collect the corresponding ECL signals. The measured signals were denoted as $I_{Hg^{2+}}$ and $I_{Ni^{2+}}$.

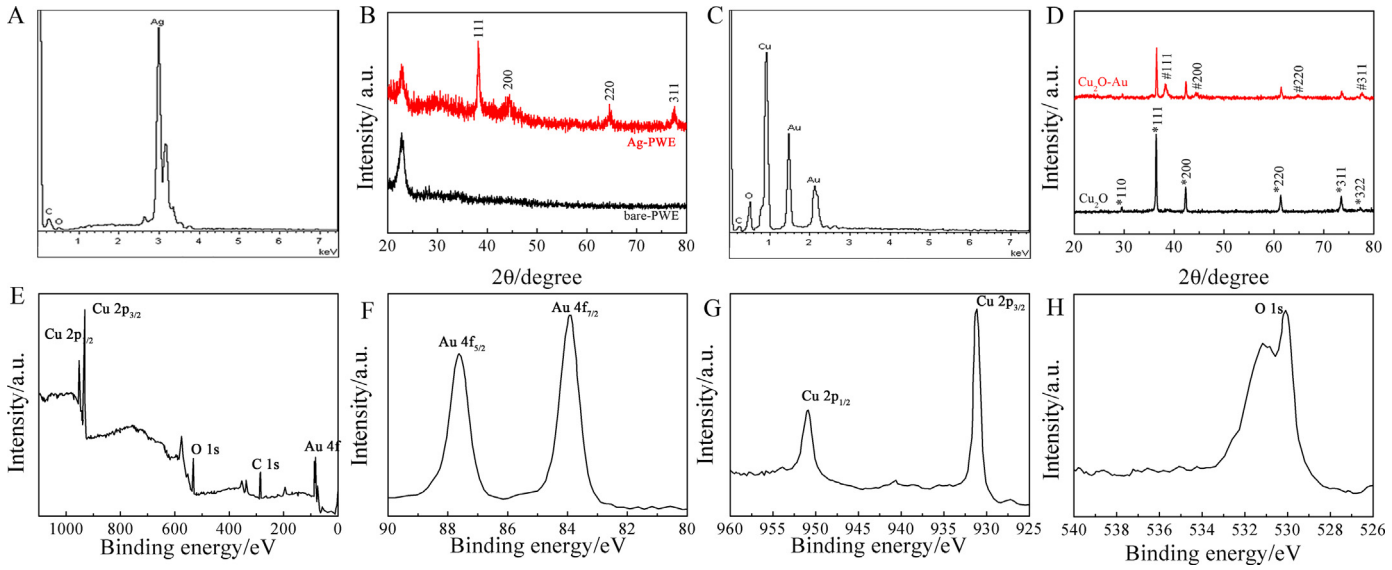

Fig. 2. EDS images of (A) Ag-PWE and (C) Cu_2O-Au. (B) XRD images of Ag-PWE and bare-PWE. (D) XRD images of Cu_2O and Cu_2O-Au. XPS spectra of Cu_2O-Au nanocomposites: (E) overview XPS spectrum of the products; (F) Au 4f spectrum; (G) Cu 2p spectrum and (H) O 1s spectrum.

3. Results and discussion

3.1. Morphology and structure studies

Fig. 1A and Fig. 1B showed scanning electron microscopy (SEM) images of the bare-PWE and as-prepared Ag-PWE, respectively. As illustrated in Fig. 1A, the bare-PWE with rough and porous cellulose fiber was observed clearly creating a unique microenvironment for the growth of the Ag NPs. Fig. 1B showed that a pyknotic and continuous layer of Ag NPs was uniformly distributed on the cellulose fiber surfaces (Fig. 1B). The morphological features of Ag NPs were directly depicted by enlarged SEM image in Fig. 1E. The Ag NPs had spherical structures with a smooth surface and large contact area. The corresponding energy dispersive spectrometer (EDS) spectrum of the Ag-PWE (Fig. 2A) gave the signals of C, O and Ag, which proved the successful synthesis of Ag-PWE. In Fig. 1F, the element mappings of C, O and Ag confirmed the elemental distribution of the Ag NPs on the surface of PWE. In order to examine the phase and structure of Ag NPs, bare-PWE and Ag-PWE were determined by X-ray diffraction (XRD) analysis. The diffraction peaks of Ag NPs were inferred by comparing the XRD patterns of bare-PWE and Ag-PWE (Fig. 2B). All the diffraction peaks around 38.23, 44.46, 64.63, and 77.63 indexed to (111), (200), (220), and (311) planes, respectively, were observed, which verified the structure of Ag NPs.

The morphological features of Cu_2O nanomaterial were directly depicted by SEM image in Fig. 1C. It was clearly found that the Cu_2O nanomaterial presented a cubic structure with a smooth surface and a diameter of about 110 nm. Compared with the pure Cu_2O, Cu_2O decorated by Au (Fig. 1D) presented a rough surface with many granules. As shown in Figs. 1G and 1H, Cu_2O and Cu_2O-Au were further characterized by transmission electron microscope (TEM). Fig. 2C showed the corresponding EDS images, which consisted of the characteristic peaks of C, O, Cu and Au, testifying that Cu_2O-Au was successfully synthesized. Further evidence was provided by the XRD analysis (Fig. 2D). The XRD pattern of Cu_2O-Au showed the diffraction peaks of Au in contrast to that of pure Cu_2O, proving the successful embellishment of Au nanoparticles. X-ray photoelectron spectroscopy (XPS) characterization was performed to investigate the chemical composition of Cu_2O-Au. As indicated in Fig. 2E, all characteristic peaks including Au 4f, Cu 2p, C 1s and O 1s were detected in the overview XPS spectrum. And the peaks located at 83.9 and 87.6 eV matched well with the values of the zero oxidation state of metallic Au, representing the existence of Au nanoparticles (Fig. 2F). Besides, the Cu $2p_{3/2}$ and Cu $2p_{1/2}$ were located at 932.48 and 952.37 eV (Fig. 2G), and the O 1s was resolved into two peaks including 530.1 eV and 531.1 eV, which confirmed the presence of Cu_2O (Fig. 2H). The C 1s peak located at 284.7 eV was ascribed to adventitious carbon presenting in the experiment. These survey results indicated that the Au NPs were successful dispersed in the surface of Cu_2O nanocube.

3.2. Mechanism analysis

In this work, PEI-ABEI, as a self-enhanced molecule of ECL intramolecular reaction, was fixed on the surface of Ag-PWE. To check on the intramolecular catalysis of PEI-ABEI, ECL responses of ABEI and PEI-ABEI were determined without H_2O_2, and corresponding experimental results were shown in Fig. 3A. It was clearly that the ECL signal of the PEI-ABEI had clearly enhanced by contrast with that of ABEI alone. Therefore, the feasibility of the intramolecular catalysis was confirmed. According to the previous report (Wang et al., 2018), the possible principle of the intramolecular catalysis of PEI-ABEI was investigated as follows: PEI and ABEI were electro-oxidized into $PEI^{\bullet+}$ and $ABEI^{\bullet-}$. The obtained products continued interacting with each other to form the excited state. When it decayed from excited state to ground state, the light was emitted, resulting in enhancement of signal.

Besides, intermolecular reaction of ABEI-H_2O_2 was further investigated. As shown in Fig. 3A, the ECL signal of ABEI-H_2O_2 system had clearly increased after the addition of Cu_2O, Cu_2O-Au, and Ag NPs. However, the ECL signal of the mixture containing ABEI, Ag NPs, and Cu_2O-Au had no obvious change compared with that of ABEI. this phenomenon indicated that Cu_2O (Xu et al., 2013), Cu_2O-Au, and Ag NPs with superior peroxidase-like activity promoted the decomposition of H_2O_2 to produce abundant reactive oxygen species (ROSs), enhancing the luminescence of ABEI. Additionally, referring to the previous literature (Wilson and Schiffrin, 1996), Fc also presented the excellent catalytic performance for H_2O_2, which further promoted the ECL emission of ABEI. And the detailed mechanism of the intermolecular reaction was shown as follows:

$$Fc - e^- \rightarrow Fc^+ \quad (1)$$

$$ABEI - e^- - 2H^+ \rightarrow ABEI^{\bullet -} \quad (2)$$

$$H_2O_2 \xrightarrow{Fc^+ Cu_2O-Au\ Ag\ NPs} OH^{\bullet} + O_2^{\bullet -} \quad (3)$$

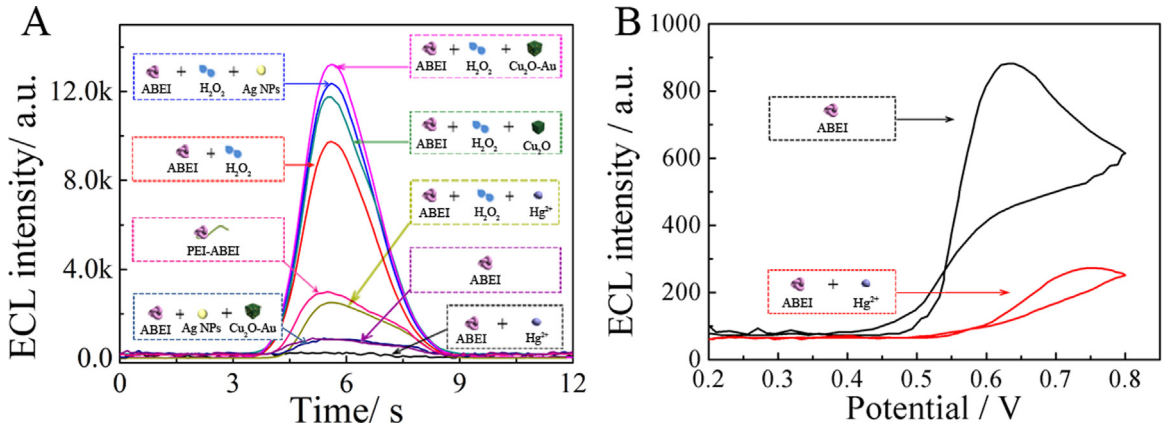

Fig. 3. (A) ECL-time curves of the working electrodes in Tris-HCl buffer with different components. (B) ECL-potential curves of the ABEI in Tris-HCl buffer (pH 7.4) with or without Hg^{2+}.

$$ABEI^{-} + OH^{\cdot}/O_2^{\cdot -} \rightarrow (ABEI_{OX})^{*} + \text{products} \quad (4)$$

$$(ABEI_{OX})^{*} \rightarrow ABEI_{OX} + h\nu \quad (5)$$

Thus, the ECL signal amplification was achieved through the integration of the intramolecular catalysis and the intermolecular co-reaction.

After the incubation of Hg^{2+}, an extremely low ECL signal was measured (Fig. S4D). To explore the quenching mechanism, the ECL intensity of ABEI solution containing Hg^{2+} was measured in the absence and presence of H_2O_2. As shown in Fig. 3A, the ECL emission of ABEI-H_2O_2 system became weak after adding Hg^{2+}. And the same situation still happened in the absence of H_2O_2. It indicated that the inhibiting effect of Hg^{2+} was not affected by H_2O_2. Fig. 3B showed that the ECL signal of ABEI began to emit at around 0.4 V and reached its maximum ECL intensity at a potential of 0.63 V. However, after the addition of Hg^{2+}, the ECL emission and the maximum ECL emission were transferred to around 0.61 V and 0.74 V, respectively. Therefore, the probable quenching reason was inferred that Hg^{2+} inhibited the oxidation of ABEI and formation of excited-state ABEI, resulting in an extremely low ECL signal and eventually achieving the quantitative analysis of Hg^{2+}.

Under the existence of Ni^{2+}, the ECL signal of ABEI had clearly decreased (Fig. S4C). And the reason of the phenomenon was the sequence of Ni^{2+}-specific DNAzyme was specially recognized and activated by Ni^{2+}. The activated DNAzyme would catalyze the ribonucleotide (rA) site in strand S2 and promote the fracture of the strand S2. After that, Fc was released from the surface of electrode, which leaded to the reduction of ECL signal. According to the mechanism of the intermolecular reaction, the ECL intensity was decreased along with the amount of Fc. And the amount of Fc had positive relationship with the concentration of Ni^{2+}. Thus, there was a negative correlation between ECL signal and the concentration of Ni^{2+}, which realized the sensitive detection of Ni^{2+}. And the corresponding mechanism of CAPEB is illustrated in Scheme S2.

3.3. Analytical performance

Based on the Ni^{2+}-specific DNAzyme and quenching effect of Hg^{2+} on ABEI, CAPEB was fabricated for ultrasensitive determination of Hg^{2+} and Ni^{2+}, respectively. The performance of CAPEB was monitored under the optimized conditions (detailed procedure was described in the Supplementary information). As shown in the inset of Figs. 4A and 4B, the ΔECL intensity ($\Delta I_{Hg^{2+}} = I_0 - I_{Hg^{2+}}$, $\Delta I_{Ni^{2+}} = I_0' - I_{Ni^{2+}}$) decreased gradually with the increasing of HMI in the clear concentration range. In Fig. 4A, the ΔECL intensity acted as a function of the logarithm of Ni^{2+} concentration. The linear regression equation was expressed as follows: $\Delta I_{Ni^{2+}} = 208.7 + 921.0 \lg c_{Ni^{2+}}$ with the regression coefficient (R^2) of 0.9912. Additionally, Fig. 4B showed that the peak currents linearly responded to the logarithmic value of Hg^{2+} concentration ranging from 10 p.M. to 1 μM. The correlation equation was $\Delta I_{Hg^{2+}} = 3990.7 + 1319.8 \lg c_{Hg^{2+}}$ ($R^2 = 0.9920$), and the detection limit was 3. 8 p.M. By contrast with other detection methods in previous report (Table S2), CAPEB represented wider linear ranges and lower limits of detection, exhibiting its superior performance in detection.

3.4. Specificity, reproducibility and stability

In this study, to evaluate the specificity of CAPEB for detection of Ni^{2+} and Hg^{2+}, the biosensor was incubated with some potential interferences, e.g., Zn^{2+}, Al^{3+}, Cu^{2+}, Fe^{3+}, and Ca^{2+}. And the corresponding results are shown in Figs. 4C and 4D. The existence of the interfering agents with higher concentration (10-fold, 10 μM) than target Ni^{2+} (1 μM) displayed no obvious effect on the ECL signal (Fig. 4C). When the CAPEB was incubated with the mixture containing Zn^{2+} (10 μM), Al^{3+} (10 μM), Cu^{2+} (10 μM), Fe^{3+} (10 μM), Ca^{2+} (10 μM), and Ni^{2+} (1 μM), the ECL intensity had no obvious difference compared with that of the only Ni^{2+} (1 μM). Similarly, the specificity for detection of Hg^{2+} was studied by incubating with Zn^{2+} (10 nM), Al^{3+} (10 nM), Cu^{2+} (10 nM), Fe^{3+} (10 nM), Ca^{2+} (10 nM), Hg^{2+} (1 nM) and mixture including target Hg^{2+} and the above interferences. As shown in Fig. 4D, the ECL signal was not affected by these interferences. Besides, so as to discuss whether there was the cross-impact, Ni^{2+} and Hg^{2+} acted as interferences each other for detection. The result indicated there was no the cross-impact between Ni^{2+} and Hg^{2+}.

The reproducibility of CAPEB was investigated through testing the concentration of target on five different biosensors. Inter-assay and intra-assay relative standard deviation (RSD) were also measured, respectively. According to the result, RSD values of Ni^{2+} detection were less than 3.4% and 4.5% for the device in same and different batch. And the RSD values of Hg^{2+} detection were less than 3.9% and 4.1%. This result was acceptable for quantitative assays performed in real samples. Moreover, the stability of the biosensor was another crucial property. After the device was stored at 4 °C for two weeks before the experiment, there was no obvious change here in the electrochemical strength, demonstrating a storage stability of the electrode.

3.5. Application of the CAPEB

To verify the practical applicability and reliability of the proposed ECL device, the detection of Hg^{2+} and Ni^{2+} were performed by dropping various concentrations of Hg^{2+} or Ni^{2+} into the lake water samples prepared by simply filtered firstly. After incubating in the lake water samples diluted with Tris-HCl buffer, the devices were tested under the optimum experimental conditions. According to the

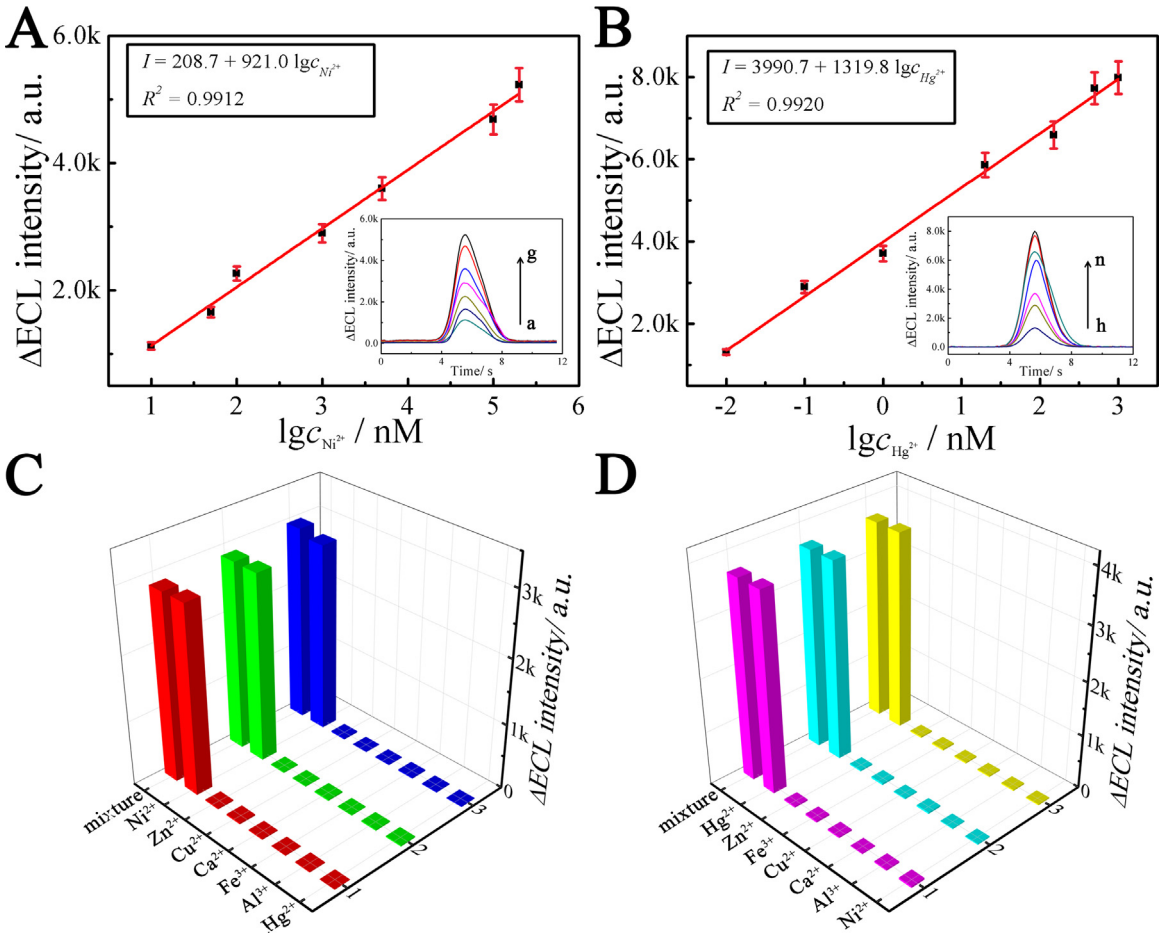

Fig. 4. (A) Calibration plots of ΔECL intrensity vs the logarithm of Ni^{2+} concentration; insert: ΔECL intrensity of the proposed biosensor with different concentrations in 20 μL 10 mM Tris-HCl buffer (pH 7.4, 1 mM H_2O_2): (a) 10 nM, (b) 50 nM, (c) 100 nM, (d) 1 μM, (e) 5 μM, (f) 100 μM, (g) 200 μM. (B) Calibration plots of ΔECL intrensity vs the logarithm of Hg^{2+} concentration; insert: ΔECL intrensity of the proposed biosensor with different concentrations in 20 μL 10 mM Tris-HCl buffer (pH 7.4, 1 mM H_2O_2): (h) 10 pM, (i) 100 pM, (j) 1 nM, (k) 20 nM, (l) 150 nM, (m) 500 nM, (n) 1 μM. (C) Selectivity investigation for Ni^{2+} detection: Zn^{2+} (10 μM), Al^{3+} (10 μM), Cu^{2+} (10 μM), Fe^{3+} (10 μM), Ca^{2+} (10 μM), Ni^{2+} (1 μM), and the mixture (containing Zn^{2+} (10 μM), Al^{3+} (10 μM), Cu^{2+} (10 μM), Fe^{3+} (10 μM), Ca^{2+} (10 μM), and Ni^{2+} (1 μM)). (D) Selectivity investigation for Hg^{2+} detection: Zn^{2+} (10 nM), Al^{3+} (10 nM), Cu^{2+} (10 nM), Fe^{3+} (10 nM), Ca^{2+} (10 nM), Hg^{2+} (1 nM) and the mixture (containing Zn^{2+} (10 nM), Al^{3+} (10 nM), Cu^{2+} (10 nM), Fe^{3+} (10 nM), Ca^{2+} (10 nM), and Hg^{2+} (1 nM)).

Table 1
Determination of heavy metal ion added in lake water samples (n = 3) with CAPEB.

Metal ion	Concentration/nm	Concentration Found/ nm	Recovery/%	RSD/%
Ni^{2+}	10	10.15	101.5	1.1
	20	20.32	101.6	0.98
	50	48.67	97.3	2.2
	100	96.40	96.4	2.0
	5000	5015.69	100.3	1.5
Hg^{2+}	0.01	0.0096	96.0	1.3
	0.1	0.104	104.0	1.9
	1	1.02	102.0	2.2
	10	10.38	103.8	0.8
	100	99.45	99.5	0.5

experimental results (Table 1), the recovery values of the Hg^{2+} or Ni^{2+} were ranging from 96.0% to 104.0% and from 96.4% to 101.6%, respectively. It proved that the proposed biosensor had good reliability and accuracy for Hg^{2+} and Ni^{2+} detection in real samples.

4. Conclusion

In this work, we integrated simple origami assembly, the hollow-channel structure, and the multiple fluidic paths into a paper device chip, realizing the simultaneous auto-cleaning of the two working electrodes, which significantly decreased multiple personnel performing procedures and shortened the measurement time. Besides, binary catalysis strategies consisting of intramolecular self-catalysis of PEI-ABEI and intermolecular co-reaction between H_2O_2 and ABEI was firstly introduced into the CAPEB, obtaining greatly enhanced ECL signal. By taking advantage of Ni^{2+}-specific DNAzyme and quenching effect of Hg^{2+} on ABEI, CAPEB realized the supersensitive detection of Ni^{2+} and Hg^{2+} with a relatively low detection limit of 3.1 nM and 3.8 pM The developed CAPEB presented fascinating analytical performance, which may provide a new avenue for designing new-type multifunctional paper-based diagnostic device.

Acknowledgements

The authors are thankful for support from the National Natural Science Foundation of China (51872121 and 21874055), the Program for Taishan Scholar of Shandong Province (ts201712048), and Major Program of Shandong Province Natural Science Foundation (ZR2017ZC0124).

Supporting information

Materials and reagents, used oligonucleotides in our present work, apparatus and measurements, design of CAPEB, preparation of materials, fabrication process of CAPEB, characterizations of the stepwise modified electrode, optimization of the experimental conditions, figures, feasibility of CAPEB, comparison of CAPEB with other methods for the detection of Hg^{2+} and Ni^{2+}, determination of metal ion added in lake water samples with CAPEB.

Appendix A. Supplementary material

Supplementary data associated with this article can be found in the online version at doi:10.1016/j.bios.2018.11.008.

References

Ajayaghosh, A., Carol, P., Sreejith, S., 2005. J. Am. Chem. Soc. 127 (43), 14962–14963.
Bao, W.-J., Li, J., Li, J., Zhang, Q.-W., Liu, Y., Shi, C.-F., Xia, X.-H., 2018. Anal. Chem. 90 (6), 3842–3848.
Cai, Y., You, J., You, Z., Dong, F., Du, S., Zhang, L., 2018. Biosens. Bioelectron. 99, 332–337.
Channon, R.B., Yang, Y., Feibelman, K.M., Geiss, B.J., Dandy, D.S., Henry, C.S., 2018. Anal. Chem.
Chen, S., Liu, P., Su, K., Li, X., Qin, Z., Xu, W., Chen, J., Li, C., Qiu, J., 2018. Biosens. Bioelectron. 99, 338–345.
Cui, L., Wu, J., Li, J., Ju, H., 2015. Anal. Chem. 87 (20), 10635–10641.
Dong, Y.-P., Wang, J., Peng, Y., Zhu, J.-J., 2017. Biosens. Bioelectron. 94, 530–535.
Fang, X., Liu, J., Wang, J., Zhao, H., Ren, H., Li, Z., 2017. Biosens. Bioelectron. 97, 218–225.
Ge, S., Zhao, J., Wang, S., Lan, F., Yan, M., Yu, J., 2018. Biosens. Bioelectron. 102, 411–417.
Ge, Y., Li, Z., 2018. ACS Sustain. Chem. Eng. 6 (5), 7181–7192.
Guo, X., Qian, X., Jia, L., 2004. J. Am. Chem. Soc. 126 (8), 2272–2273.
Hai, J., Chen, F., Su, J., Xu, F., Wang, B., 2018. Anal. Chem. 90 (7), 4909–4915.
Hua, Q., Shi, F., Chen, K., Chang, S., Ma, Y., Jiang, Z., Pan, G., Huang, W., 2011. Nano Res. 4 (10), 948–962.
Huang, R.J., Zhang, Y., Bozzetti, C., Ho, K.F., Cao, J.J., Han, Y., Daellenbach, K.R., Slowik, J.G., Platt, S.M., Canonaco, F., Zotter, P., Wolf, R., Pieber, S.M., Bruns, E.A., Crippa, M., Ciarelli, G., Piazzalunga, A., Schwikowski, M., Abbaszade, G., Schnelle-Kreis, J., Zimmermann, R., An, Z., Szidat, S., Baltensperger, U., El Haddad, I., Prevot, A.S., 2014. Nature 514 (7521), 218–222.
Huang, X., Zhou, Y., Liu, C., Zhang, R., Zhang, L., Du, S., Liu, B., Han, M.-Y., Zhang, Z., 2016. Biosens. Bioelectron. 86, 530–535.
Ke, H., Zhang, X., Huang, C., Jia, N., 2018. Biosens. Bioelectron. 103, 62–68.
Koley, P., Sakurai, M., Aono, M., 2016. ACS Appl. Mater. Interface 8 (3), 2380–2392.
Kong, Q., Wang, Y., Zhang, L., Xu, C., Yu, J., 2018. Biosens. Bioelectron. 110, 58–64.
Li, L., Zhang, Y., Zhang, L., Ge, S., Liu, H., Ren, N., Yan, M., Yu, J., 2016. Anal. Chem. 88 (10), 5369–5377.
Li, L., Zhang, Y., Zhang, L., Ge, S., Yan, M., Yu, J., 2017. Sci. Bull. 62 (16), 1114–1121.
Li, S.-K., Liu, Z.-T., Li, J.-Y., Chen, A.-Y., Chai, Y.-Q., Yuan, R., Zhuo, Y., 2018. ACS Appl. Mater. Interface 10 (17), 14483–14490.
Liu, D., Li, Z., Li, W., Zhong, Z., Xu, J., Ren, J., Ma, Z., 2013. Ind. Eng. Chem. Res. 52 (32), 11036–11044.
Liu, M., Zhang, H., Shu, J., Liu, X., Li, F., Cui, H., 2014. Anal. Chem. 86 (6), 2857–2861.
Liu, X.W., 2011. Langmuir 27 (15), 9100–9104.
Martinez, A.W., Phillips, S.T., Whitesides, G.M., Carrilho, E., 2010. Anal. Chem. 82 (1), 3–10.
Miao, P., Tang, Y., Wang, L., 2017. ACS Appl. Mater. Interface 9 (4), 3940–3947.
Susman, M.D., Feldman, Y., Vaskevich, A., Rubinstein, I., 2014. ACS Nano 8 (1), 162–174.
Wang, H., Chai, Y., Li, H., Yuan, R., 2018. Biosens. Bioelectron. 100, 35–40.
Weng, X., Neethirajan, S., 2018. J. Food Saf. 38 (1), e12412.
Wilson, R., Schiffrin, D.J., 1996. Anal. Chem. 68 (7), 1254–1257.
Xie, J., Zheng, Y., Ying, J.Y., 2010. Chem. Commun. 46 (6), 961–963.
Xu, F., Deng, M., Li, G., Chen, S., Wang, L., 2013. Electrochim. Acta 88, 59–65.
Xu, S., Sun, S., Chen, G., Song, X., 2009. J. Cryst. Growth 311 (9), 2742–2745.
Yan, Z., Wang, F., Deng, P., Wang, Y., Cai, K., Chen, Y., Wang, Z., Liu, Y., 2018. Biosens. Bioelectron. 109, 132–138.
Yang, H., Zhang, Y., Li, L., Zhang, L., Lan, F., Yu, J., 2017. Anal. Chem. 89 (14), 7511–7519.
Yang, H., Zhang, Y., Zhang, L., Cui, K., Ge, S., Huang, J., Yu, J., 2018a. Anal. Chem. 90 (12), 7212–7220.
Yang, X., Yu, Y.-Q., Peng, L.-Z., Lei, Y.-M., Chai, Y.-Q., Yuan, R., Zhuo, Y., 2018b. Anal. Chem. 90 (6), 3995–4002.
Zhang, L., Han, Y., Zhao, F., Shi, G., Tian, Y., 2015. Anal. Chem. 87 (5), 2931–2936.
Zhang, M., Ge, L., Ge, S., Yan, M., Yu, J., Huang, J., Liu, S., 2013. Biosens. Bioelectron. 41, 544–550.
Zhang, S., Zhang, D., Zhang, X., Shang, D., Xue, Z., Shan, D., Lu, X., 2017a. Anal. Chem. 89 (6), 3538–3544.
Zhang, Y., Li, L., Zhang, L., Ge, S., Yan, M., Yu, J., 2017b. Nano Energy 31, 174–182.
Zheng, X., Li, L., Cui, K., Zhang, Y., Zhang, L., Ge, S., Yu, J., 2018. ACS Appl. Mater. Interface 10 (4), 3333–3340.